Chinese Journal of Chemical Engineering 76 (2024) 281–291

Contents lists available at ScienceDirect

Chinese Journal of Chemical Engineering

journal homepage: www.elsevier.com/locate/CJChE

Full Length Article

Effect of cobalt on the activity of nickel-based/magnesium-substituted hydroxyapatite catalysts for dry reforming of methane

Tongming Su [1], Bo Gong [1], Xinling Xie [1], Xuan Luo [1], Zuzeng Qin [1,*], Hongbing Ji [1,2]

[1] School of Chemistry and Chemical Engineering, Guangxi University, Nanning 530004, China
[2] Zhejiang Green Petrochemical and Light Hydrocarbon Transformation Research Institute, Zhejiang University of Technology, Hangzhou 310014, China

ARTICLE INFO

Article history:
Received 14 April 2024
Received in revised form
21 July 2024
Accepted 22 July 2024
Available online 28 September 2024

Keywords:
Methane
Carbon dioxide
Hydroxyapatite
Nickel
Cobalt

ABSTRACT

The dry reforming of methane (DRM) reaction can directly convert methane (CH_4) and carbon dioxide (CO_2) into syngas (H_2+CO), which is a promising method for achieving carbon neutralization. In this study, a series of 3Ni-*x*Co/Mg_1HAP alloy catalysts with different ratio were synthesized by the coprecipitation method, and the optimum Ni–Co ratio for the DRM reaction was studied. A series of characterization methods revealed that after Co was added, the formation of Ni–Co alloys increased the interactions between metals. However, an excess of Co inhibits the entry of Ni into the lattice of Mg_1HAP, resulting in metal accumulation on the surface of the support. In addition, the introduction of Co improves the dispersion of Ni metal, which endows the catalyst with better catalytic activity and stability. Raman spectroscopy of the catalyst after the stability test showed that the addition of Co reduced the proportion of graphitic carbon, which was also the main reason for its improved stability.

1. Introduction

In recent years, the problem of global warming has attracted increasing amounts of attention, and methane and carbon dioxide, two greenhouse gases, are the main causes of global warming; moreover, carbon neutralization strategies have been widely implemented worldwide [1–7]. Dry reforming of methane is a very effective method. It directly uses carbon dioxide (CO_2) and CH_4, two greenhouse gases, and converts them into syngas (H_2+CO) [8,9]. Syngas can be applied in the Fischer–Tropsch reaction (FTS) to produce methanol or other fuel resources, which can convert low-value-added chemicals into high-value-added chemicals [10,11].

Ni-based catalysts are considered to be the most practical potential dryreforming of methane (DRM) catalysts because they are less expensive and have the same catalytic activity as precious metals (Ir, Rh, Ru, Pt, and Pd) [12–17]. However, catalyst coking and active metal Ni sintering are the main challenges for the commercial application of Ni-based catalysts [18–20]. The sintering of metal Ni occurs mainly through the agglomeration of metal Ni into larger metal Ni particles under high-temperature reduction and high-temperature reaction conditions [21,22], while CH_4 tends to decompose excessively on larger Ni particles ($CH_4 \rightarrow C+4H^*$), resulting in carbon deposition [23–25]. Therefore, a useful way to solve the problems of carbon deposition and metal sintering is to reduce the size of metal nanoparticles and enhance the interaction between the metal and support [26,27]. A large number of published reports show that when the size of metal nanoparticles is less than a certain threshold, they can inhibit the nucleation of graphitized carbon and effectively prevent carbon deposition [28–30]. He *et al.* [31] prepared γ-Al_2O_3-supported ultrafine Ni nanoparticle (3.7 nm) catalysts, which showed remarkable stability to CH_4 and CO_2 at 700 °C, and the CH_4 conversion decreased by only 9.6 % after 20 h of reaction. Wang *et al.* [32] encapsulated bimetallic Ni nanoparticles (2.8 nm) in silicalite-2. They found that the reaction showed high resistance to carbon deposition even at 650 °C, where severe coking would occur. Metal sintering occurs due to the migration of metal nanoparticles, so it is highly important to enhance the interaction between the metal and support to improve the sintering resistance of metals. It has been proven that the alloying effect can induce stronger metal-support interactions in the reported literature. Because Ni and Co have similar electronic structures, it is very easy to form Ni–Co alloys.

One of the main reasons for the easy deactivation of Ni-based monometallic catalysts is that they have high activity against the C–H orbital of CH_4 [23], which leads to the continuous accumulation of carbon species (C*) in the active sites, which eventually leads to deactivation of the catalysts. The addition of a second

* Corresponding author.
E-mail address: qinzuzeng@gxu.edu.cn (Z. Qin).

https://doi.org/10.1016/j.cjche.2024.07.025

metal can effectively alleviate this situation, and the addition of a second metal will also improve the metal-support interaction [33,34]. The addition of the second metal promotes electron transfer between Ni and the second metal, which is beneficial for the formation of oxygen species (O*). O* oxidizes the C* produced by CH_4 cracking into CO, thus preventing the accumulation of C* on the surface of the metal Ni [35,36]. However, the excessive addition of a second metal will produce excessive O*, which will lead to the oxidation of the metal and decrease the activity of the catalyst. Therefore, the introduction of an appropriate amount of second metal is beneficial for inhibiting the coking and sintering of the catalyst. Metal Co has been widely studied as a second metal because of its high oxophilicity and high activity [37]. Erdogan *et al.* prepared Ni@SBA-15, Co@SBA-15, and Ni—Co@SBA-15 by wet impregnation. The results showed that due to the formation of the Ni—Co alloy, the Ni—Co@SBA-15 catalyst effectively inhibited the agglomeration of the Ni particles. The activity test results showed that the bimetallic catalyst promoted the formation of O* on the surface of the catalyst due to the electron transfer between Ni and Co, thus inhibiting the accumulation of carbon [38]. AlSabban *et al.* [39] studied the CH_4 and CO_2 activation equilibrium of Co, Ni, and different proportions of Ni—Co alloy catalysts. The results showed that the carbon deposition produced by the Ni—Co alloy catalysts during the DRM process was negligible. Density functional theory calculations revealed that, compared with the pure Ni and Co catalysts, the Ni—Co alloy catalysts exhibited moderate oxygen chemical adsorption energy. The adsorption energy of O* species increases with increasing Co content, which is the main reason why the carbon deposition of Ni—Co catalysts can be ignored. Sheng *et al.* [40] studied the activation equilibrium of CH_4 and CO_2 in a Ni—Co alloy *via* DRM, focusing on the effect of the Ni—Co ratio on the carbon balance. The results showed that only by optimizing the Ni—Co ratio could the dynamic balance between CH_4 cracking and CO_2 reduction be maintained, carbon deposition on the surface of the catalyst could be prevented, and the oxidation of active metals could be alleviated. The Ni—Co alloy composition is significant for ensuring efficient and stable DRM reactions and enhancing the catalytic performance of the catalyst [41–43].

In previous work [44], using the ion exchange capacity of hydroxyapatite (HAP), Mg was used to partially replace Ca in HAP to prepare the Ni/Mg_xHAP catalyst, and the optimal amount of Mg substitution was determined. In the present study, Mg_1HAP-supported Ni—Co bimetallic catalysts were prepared by the coprecipitation method, and the best Ni—Co ratio was determined. The formation of the Ni—Co alloy and the reduction ability, dispersibility, and surface alkalinity of the catalyst were investigated *via* characterization. Finally, the stability of the catalyst was evaluated under the same reaction conditions. The Ni—Co alloy effectively promoted the cleavage of C—H and C—O and decreased the distance between O* and C*, thereby increasing the conversion of CH_4 and CO_2 and inhibiting carbon deposition.

2. Experimental

2.1. Catalyst preparation

Mg-substituted hydroxyapatite was prepared by the coprecipitation method. Mg-substituted HAP nanoparticles with a stoichiometric ratio were usually synthesized by $Ca(NO_3)_2{\cdot}4H_2O$ and $NH_4H_2PO_4$ coprecipitation methods and were named $Mg_1Ca_9(PO_4)_6(OH)_2$. $Ca(NO_3)_2{\cdot}4H_2O$ (4.25 g) and $Mg(NO_3)_2{\cdot}6H_2O$ (0.51 g) are usually mixed and dissolved in 80 ml of deionized water, and 1.38 g of $NH_4H_2PO_4$ is also dissolved in 80 ml of deionized water. A white suspension was obtained by adding $NH_4H_2PO_4$ solution to a mixture of calcium nitrate and magnesium nitrate at room temperature. The suspension was stirred at 90 °C for 3 h. The precipitates in the suspension were centrifuged, washed to neutral, and then air-dried at 80 °C overnight. The dried sample was calcined in a muffle furnace at 400 °C for 4 h to obtain the Mg_1HAP support.

Loading of Ni and Co on the Mg_1HAP support: The 0.60 g Mg_1HAP support was stirred for 10 min in 60 ml deionized water to mix the Mg_1HAP support evenly in deionized water. Subsequently, 0.5 $mol{\cdot}L^{-1}$ $Ni(NO_3)_2$ aqueous solution was added to achieve a nickel loading amount of 3 %(mass), and then 0.5 $mol{\cdot}L^{-1}$ $Co(NO_3)_2$ aqueous solution was added to achieve Co loading amounts of 1%, 2%, 3%, 4%, and 5 %(mass). The pH of the mixed solution was adjusted to 10.5 with 25 %(vol) ammonia, and the mixture was stirred at 350 $r{\cdot}min^{-1}$ for 3 h to obtain a light green precipitate. The light green precipitate was filtered and washed to make the precipitate neutral and dried overnight in an oven at 80 °C. The dried sample was calcined in a muffle furnace at 500 °C for 4 h to obtain a Ni—Co/Mg_1HAP catalyst with a Ni loading of 3 % and a Co loading of 1% to 5%.

2.2. Characterization of the catalysts

X-ray diffraction (XRD) patterns were obtained on a Rigaku D/MAX 2500 V (Rigaku, Tokyo, Japan) X-ray powder diffractometer with Cu K_α radiation. The scanning step was 0.01°, the scanning speed was 10 (°)·min^{-1}, and the data were collected from 10° to 80°. N_2 adsorption-desorption was tested on a TriStar II surface area and porosity analyzer (Micromeritics Instrument Corporation, Norcross, GA, USA), where the sample to be tested was first degassed at 300 °C for 4 h, and the surface area was calculated using the Brunauer–Emmett–Teller (BET) equation. X-ray photoelectron spectroscopy (XPS) was carried out on a Thermo Science *K*-Alpha (Thermo Fisher Scientific, Waltham, MA, USA, Al K_α $h\nu$ = 1486.6 eV). All binding energies (BEs) were calibrated using C 1s (284.8 eV) as a standard. Temperature-programmed reduction (H_2-TPR) was carried out on an AMI-300 instrument (Altamira Instruments, Cumming, GA, USA), and 50 mg samples were placed in a U-shaped quartz reactor, pretreated in 30 $ml{\cdot}min^{-1}$ flowing Ar at 573 K for 30 min, ramped to 1073 K at 10 °C·min^{-1} in 50 $ml{\cdot}min^{-1}$ flowing 10 % (vol) H_2/Ar and reacted with H_2 detected by TCD. SEM images were obtained on a Hitachi SU8220 field emission scanning electron microscope (Hitachi, Tokyo, Japan). Thermogravimetric analysis (TGA) was conducted on a thermogravimetric analyzer (Mettler Toledo, USA) to measure carbon deposition on the catalyst at 800 °C in air. Raman spectra were obtained with a HORIBA Scientific LabRAM HR Evolution spectrometer (HORIBA, France) with an excitation wavelength of 532 nm.

2.3. DRM reaction

The DRM reaction was conducted following the procedure in our previous work [45]. A total of 0.04 g of catalyst diluted with 0.60 g of quartz sand was loaded in a U-shaped quartz tube reactor with an inner diameter of 7 mm and an outer diameter of 9 mm. Before the reaction, the catalyst was reduced in 30 $ml{\cdot}min^{-1}$ 10 % H_2/Ar mixed gases at 750 °C for 40 min. With 30 $ml{\cdot}min^{-1}$ feed gas (composed of CH_4, CO_2, and N_2 with a volume ratio of 1:1:1), the DRM reaction was carried out at 750 °C for 8 h (GHSV = 45000 $ml{\cdot}g^{-1}{\cdot}h^{-1}$).

The CO_2 and CH_4 conversion, syngas ratio, H_2 yield, H_2 and CO selectivity and carbon balance were calculated using Eqs. (1)–(7), respectively.

$$X_{CO_2} = \frac{F_{CO_{2,in}} - F_{CO_{2,out}}}{F_{CO_{2,in}}} \times 100\% \quad (1)$$

$$X_{CH_4} = \frac{F_{CH_{4,in}} - F_{CH_{4,out}}}{F_{CH_{4,in}}} \times 100\% \quad (2)$$

$$R_{\frac{H_2}{CO}} = \frac{F_{H_{2,out}}}{F_{CO,out}} \quad (3)$$

$$H_2\ \text{Yield} = \frac{F_{H_{2,out}}}{2 \times F_{CH_{4,in}}} \times 100\% \quad (4)$$

$$H_2\ \text{Selectivity} = \frac{F_{H_{2,out}}}{2\left(F_{CH_{4,in}} - F_{CH_{4,out}}\right)} \times 100\% \quad (5)$$

$$\text{CO Selectivity} = \frac{F_{co,out}}{\left(F_{CH_{4,in}} - F_{CH_{4,out}}\right) + \left(F_{CO_{2,in}} - F_{CO_{2,out}}\right)} \times 100\% \quad (6)$$

$$X_C = \frac{F_{CH_{4,out}} + F_{CO_{2,out}} + F_{CO_{out}}}{F_{CH_{4,in}} + F_{CO_{2,in}}} \times 100\% \quad (7)$$

where $F_{CO_{2,in}}$, $F_{CO_{2,out}}$, $F_{CH_{4,in}}$, and $F_{CH_{4,out}}$ are the flows of the feed gases CO_2 and CH_4 in and out of the reactor, $ml \cdot min^{-1}$, respectively, and $F_{H_{2,out}}$ and $F_{CO_{out}}$ are the flows of the vent gases H_2 and CO, $ml \cdot min^{-1}$, respectively.

F_{in} is controlled by the mass flowmeter of the AMI-300 reactor (Altamira Instruments, USA). F_{out} is calculated by Agilent 8890 gas chromatograph (Agilent, USA) as follows: with N_2 as the internal standard substance, the linear relationship between flow ratio (F_t/F_{N_2}, $t = CH_4$, CO_2, CO, and H_2) and peak area ratio (At/AN_2, $t = CH_4$, CO_2, CO, and H_2) was obtained. Thus, the F_{out} of different gases at the outlet of the AMI-300 reactor can be calculated according to the ratio of different gases and N_2 in the real-time product of the reaction.

3. Results and Discussion

3.1. Support and fresh catalyst characterization

3.1.1. XRD analysis

To study the structure of the catalyst after the addition of Co and the existing forms of Ni and Co in the catalyst, catalysts with different Ni—Co ratio were characterized *via* XRD, as shown in Fig. 1. The diffraction peaks corresponding to the hydroxyapatite phase were detected at $2\theta = 25.9°$ (0 0 2), 31.8° (2 1 1), 32.2° (3 0 0), 32.9° (2 0 2), 46.8° (2 2 2), 49.7° (2 1 3), and 53.0° (0 0 4) for all the catalysts, indicating that the structure of the support did not change obviously after loading with Ni metal. The characteristic peaks of Co_3O_4 were not detected for the 3Ni/Mg1HAP, 3Ni—1Co/Mg_1HAP and 3Ni—2Co/Mg_1HAP catalysts at 36.7° and 44.3°, which may be due to the formation of $NiCo_2O_4$ [46], while the $NiCo_2O_4$ was highly dispersed on the surface of the support, so the characteristic peaks of the metals Co and $NiCo_2O_4$ could not be detected. When the content of metal Co increases to 3 %, the characteristic peaks of Co_3O_4 and $NiCo_2O_4$ appear at 36.7° and 44.3°, respectively. This may be because the excess Co is dispersed on the surface of the support in the form of oxides. The intensity of the characteristic peak of Co_3O_4 increases gradually with increasing Co_3O_4 content. This may lead to uneven dispersion of the metal Co and agglomeration to form larger Co particles at high temperature. In addition, metal Co species have a strong oxygen affinity, which easily combines with oxygen and is oxidized [47,48], resulting in deactivation of the catalyst.

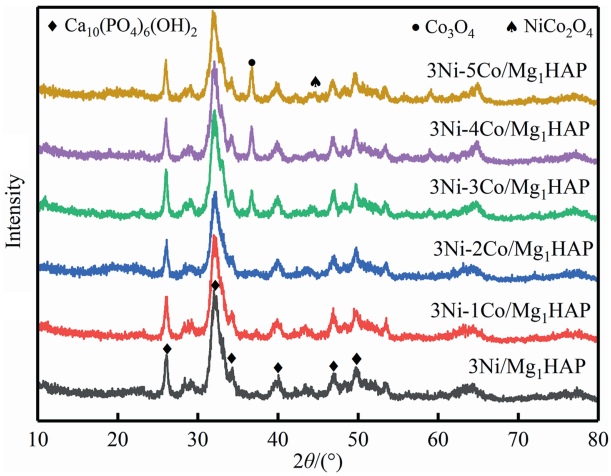

Fig. 1. XRD patterns of calcined catalysts with different Ni—Co ratio.

3.1.2. N_2 adsorption-desorption analysis

To study the effect of the second metal Co on the specific surface area, pore size and pore volume of the catalyst, N_2 adsorption-desorption experiments were carried out on several catalysts with different Ni—Co ratio, and the results are shown in Fig. 2. Fig. 2(a) shows that all the catalysts exhibit H_2 hysteresis and V-type adsorption isotherms, indicating the existence of mesopores and an ink bottle pore structure. The diagram shows that the N_2 adsorption capacity of all the samples decreased slowly with increasing relative pressure, and the hysteresis loop decreased gradually, indicating that the ability of the catalyst to adsorb N_2 decreased. This phenomenon became more obvious with increasing Co content, indicating that the Co metal blocked the pores of the catalyst, resulting in a decrease in the ability of the catalyst to adsorb N_2. Fig. 2(b) shows the pore size distributions of several catalysts for the Ni—Co/Mg_1HAP catalyst. The pore size distribution of the 3Ni/Mg_1HAP catalyst without Co is approximately 45 nm. With the addition of Co metal, the pore size of the catalyst increases to approximately 50—70 nm. When the addition of Co reached 4%, the pore size distribution of the catalyst was approximately a straight line. Combined with the isotherm data of the catalyst, it can be found that the hysteresis loop decreases with increasing Co addition. The results showed that the pore size distribution on the surface of the catalyst became wider with increasing Co addition, which was mainly because most of the pores were blocked by metal Co. Table 1 shows the specific surface area, pore volume and average pore size of several Ni-*x*Co/Mg_1HAP catalysts with different Ni—Co ratio. The table shows that the specific surface area, pore volume and average pore size of the 3Ni/Mg_1HAP catalyst without Co are 103 $m^2 \cdot g^{-1}$, 0.6 $m^3 \cdot g^{-1}$, and 19.2 nm, respectively. The specific surface area and pore volume of the catalyst decrease rapidly after the addition of the second metal Co, and this phenomenon becomes more obvious with increasing Co addition [49,50] (see Table 1).

3.1.3. H_2-TPR analysis

The effect of the second metal Co on the reduction performance of the 3Ni-x Co/Mg_1HAP catalyst was studied by H_2-TPR characterization, the results were shown in Fig. 3 and Table 2. From Fig. 3, the peak at 380 °C is attributed to the reduction of the dispersed NiO particles on the surface of the Mg_1HAP, and the peak at 512 °C is

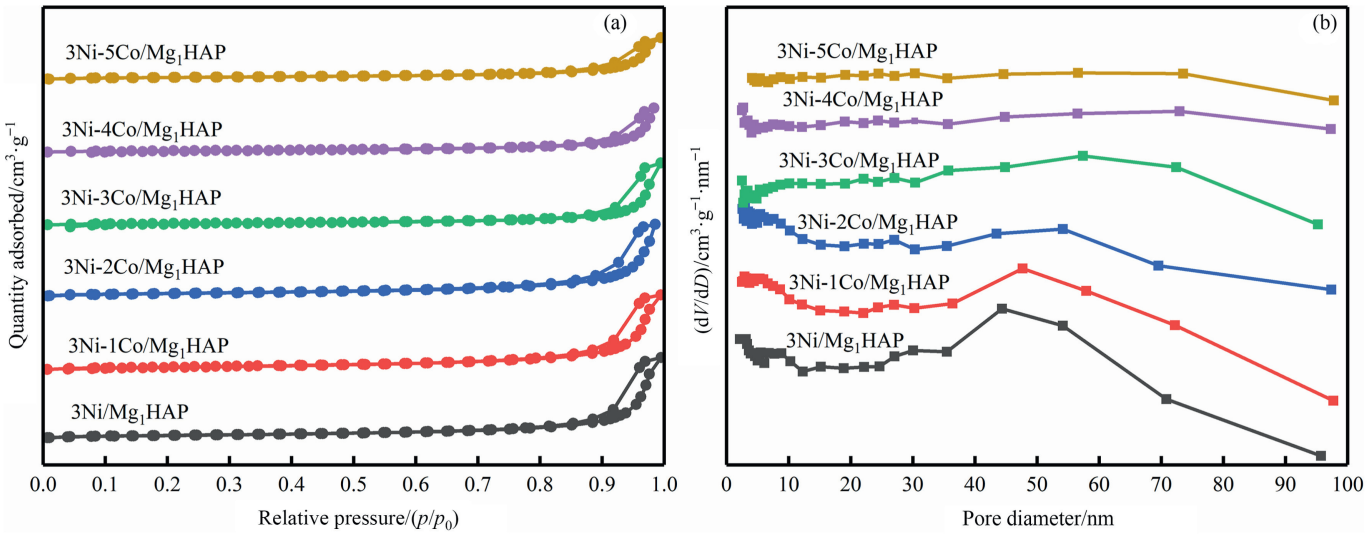

Fig. 2. N_2 adsorption-desorption isotherms (a) and pore size distributions (b) of the catalysts with different Ni–Co ratio.

Table 1
Textural properties of catalysts with different Ni–Co ratio.

Samples	$S_{BET}/m^2 \cdot g^{-1}$	Pore volume/$cm^3 \cdot g^{-1}$	Pore size/nm
3Ni/Mg_1HAP	103	0.6	19.2
3Ni–1Co/Mg_1HAP	82	0.5	20.6
3Ni–2Co/Mg_1HAP	79	0.5	17.1
3Ni–3Co/Mg_1HAP	51	0.4	16.3
3Ni–4Co/Mg_1HAP	48	0.3	15.7
3Ni–5Co/Mg_1HAP	42	0.3	14.5

Table 2
H_2 consumption of catalysts with different Ni–Co ratio.

Sample	H_2 Consumption[①]/$\mu mol \cdot g^{-1}$
3Ni/Mg_1HAP	1498
3Ni–1Co/Mg_1HAP	1369
3Ni–2Co/Mg_1HAP	1679
3Ni–3Co/Mg_1HAP	1776
3Ni–4Co/Mg_1HAP	1977
3Ni–5Co/Mg_1HAP	2158

[①] H_2 consumption calculated from TPR peaks.

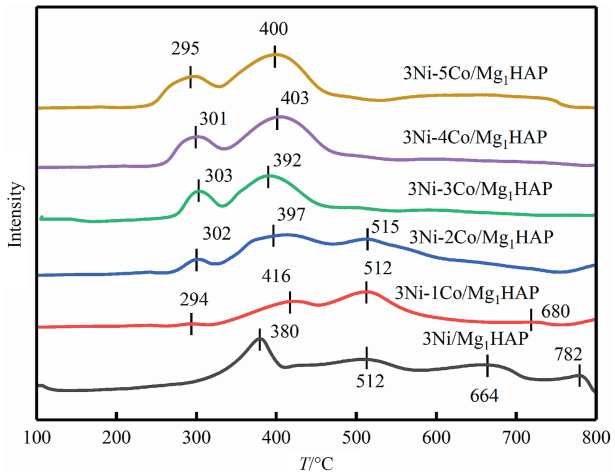

Fig. 3. H_2-TPR profiles of catalysts with different Ni–Co ratio.

ascribed to the Ni species (Ni [I]), which exchange the Ca^{2+} [I] sites in Mg_1HAP. Two peaks were found at 664°C and 782 °C, corresponding to the Ni species (Ni [II]) that exchange the Ca^{2+} [I] sites in Mg_1HAP [51]. With the addition of Co, the reduction peak at approximately 300 °C is attributed to the reduction of Co_3O_4 to CoO and subsequent reduction of CoO to metallic Co [52,53], and the peak area of the reduction peak increases with increasing Co content, indicating that more Co_3O_4 species accumulate on the support surface, which may lead to the agglomeration of metal Co species on the support surface at high temperature. After adding Co, the reduction peak of NiO shifts to approximately 400 °C, which is attributed to the formation of $NiCo_2O_4$ and the enhancement of metal-support interactions.

For the 3Ni–1Co/Mg_1HAP and 3Ni–2Co/Mg_1HAP catalysts, the peak around 510 °C belongs to the reduction of Ni^{2+} [I] species in the support lattice, and the peak at 680 °C belongs to the reduction of Ni^{2+} [II] species. With increasing Co loading, the reduction peaks of the Ni^{2+} [I] species and Ni^{2+} [II] species disappear, which may be due to the preferential combination of Co and Ni to form a Ni–Co alloy, thus inhibiting the entry of Ni metal into the HAP lattice. However, when the loading of Co reaches 5 %, a wide reduction peak appears at 550 °C and 750 °C. This reduction peak may be because excess Co enters the HAP lattice and forms a strong metal-support interaction with the support to reduce the Co species [54]. In addition, as shown in Table 2, the H_2 consumption of 3Ni–1Co/Mg_1HAP is the least, indicating that the metal in 3Ni–1Co/Mg_1HAP sample has the strongest interaction with the support, which is conducive to enhance the resistance to sintering.

3.1.4. XPS analysis

To study the change in the metal valence state in the catalyst after the addition of the second metal Co, XPS tests were carried out on the catalysts with different Ni–Co ratio. The results are shown in Fig. 4. As shown in Fig. 4(a), all the catalysts have a satellite peak at a binding energy of 860.9 eV, and for the 3Ni/Mg_1HAP catalysts, there are peaks near binding energies of 854.0 eV, 855.1, and 855.8 eV, indicating that there are at least three binding modes between the Ni on the catalyst and the support. The peak at 854.0 eV was attributed to the dispersion of NiO on the Mg_1HAP support, the peak at 855.1 eV was attributed to the Ni^{2+} [I] species formed by the Ca^{2+} [I] site in the Ni^{2+} exchange Mg_1HAP, and the peak at 855.8 eV was attributed to the Ni^{2+} [II] species formed by the Ca^{2+} [II] site in

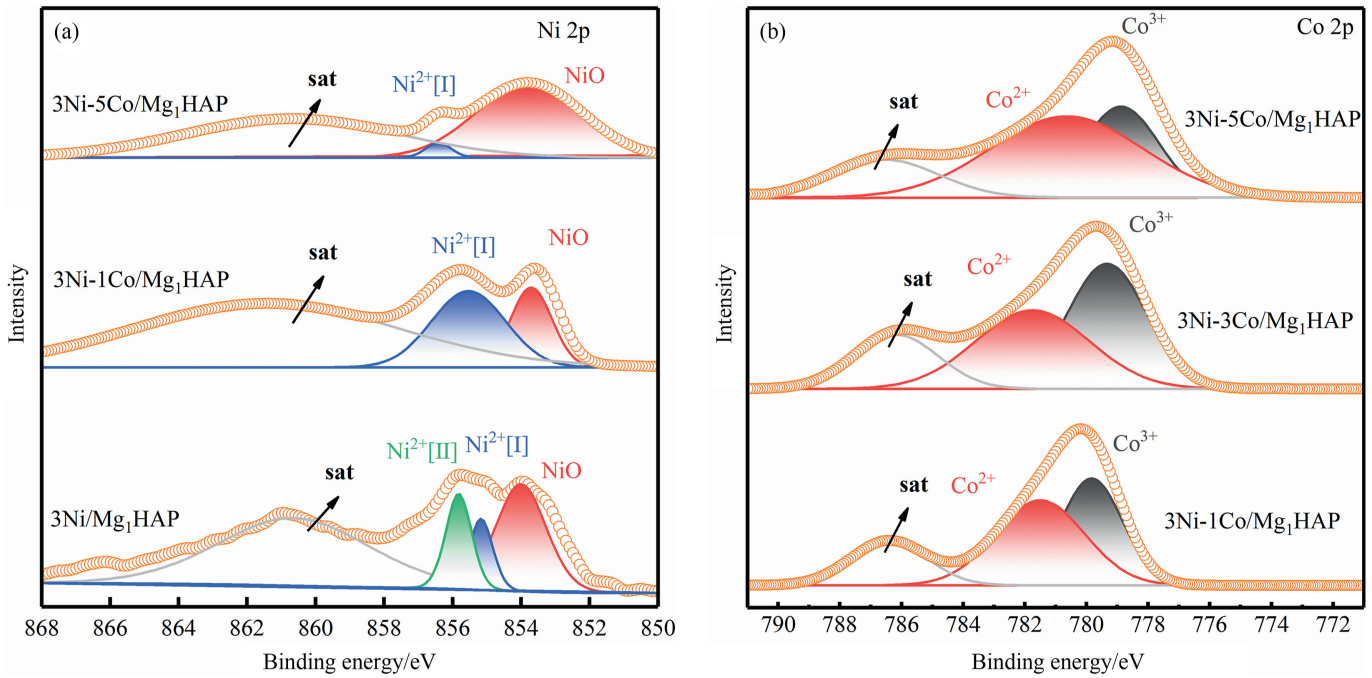

Fig. 4. (a) Ni 2p and (b) Co 2p XPS profiles of catalysts with different Ni–Co ratio.

the Ni^{2+} exchange Mg_1HAP. Therefore, Ni^{2+} ions enter the lattice of Mg_1HAP to replace Ca^{2+} on the surface of Mg_1HAP. Moreover, Mg^{2+} preferentially substitutes the Ca^{2+} [II] site in HAP, and the ionic radius of Mg is smaller than that of Ca, which results in lattice distortion and a large number of lattice defects in HAP, thus prompting Ni^{2+} to substitute for the Ca^{2+} [II] site. The difference in the binding energy of the peaks of the two Ni^{2+} species is attributed to the difference in coordination formed by the exchange of Ni^{2+} at the Ca^{2+} [I] and Ca^{2+} [II] sites. For the 3Ni–1Co/Mg_1HAP and Ni–5Co/Mg_1HAP catalysts, the peak attributed to the Ni^{2+} [II] binding energy disappears. The binding energy of the Ni^{2+} [I] species decreases with increasing Co content, while the binding energy of the NiO peak at 854.0 eV increases gradually, indicating that the metal Ni binds preferentially after the addition of Co, which leads to a decrease in the metal Ni content in the Mg_1HAP support. However, the content of NiO on the surface of the support increased, which was consistent with the H_2-TPR results.

To further study the formation of the Ni–Co alloy after the addition of the second metal Co, several catalysts with metal Co were analyzed by XPS, as shown in Fig. 4(b). The three catalysts shown in Fig. 4(b) all have three peak positions. There is a satellite peak near the binding energy of 786.5 eV. The peaks located near 781.5 and 780 eV are attributed to Co^{2+} and Co^{3+} [55–57] in the XPS spectra of 3Ni–1Co/Mg_1HAP. When the Co content reaches 5 %, the Co^{2+} binding energy clearly shifts in the direction of decreasing binding energy. This may be because Co^{2+} enters the lattice of the support, resulting in a change in the binding mode of Co^{2+} in the catalyst, so its binding energy changes [40]. In addition, after adding Co, the peak of Ni^{2+} [II] at 855.8 eV disappeared, and the intensity of the Ni^{2+} [I] peak decreased with increasing Co amount, indicating that Co preferentially interacts with Ni at the Ca^{2+} [II] site and ultimately inhibits the entry and exchange of Ni into the Mg_1HAP lattice. With the addition of Co, the peak of Ni^{2+} [I] shifted toward the direction of increasing binding energy, while the peaks of Co^{3+} and Co^{2+} shifted toward the direction of decreasing binding energy, indicating that the electrons of the Ni^{2+} species were transferred to Co, confirming the formation of a Ni–Co alloy [58]. Furthermore, the large shift in the Ni^{2+} species peak confirmed the strong interaction between Ni and Co.

3.1.5. CO_2-TPD analysis

The effect of the addition of the second metal Co on the acidity and basicity of the catalyst was studied by CO_2-TPD. The results are shown in Fig. 5. The CO_2 desorption amounts of catalysts with different Ni–Co ratio are listed in Table 3. Fig. 5 shows the CO_2-TPD spectra of freshly prepared catalysts with different Ni–Co ratio. There are broad peaks produced by multipeak overlap in the range of 25–600 °C. After the CO_2-TPD spectra of several catalysts were separated, the wide peaks could be divided into three CO_2

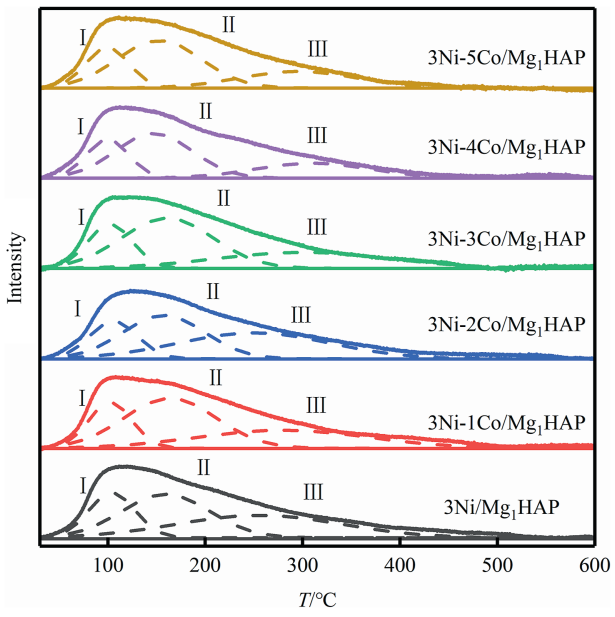

Fig. 5. CO_2-TPD profiles of the reduced catalysts.

Table 3
The amount of CO_2 desorbed from the catalysts with different Ni–Co ratio

Sample	CO_2 desorption amount/μmol·g^{-1}			
	Type I	Type II	Type III	Total
3Ni/Mg_1HAP	46	83	79	208
3Ni–1Co/Mg_1HAP	31	122	116	269
3Ni–2Co/Mg_1HAP	75	99	105	279
3Ni–3Co/Mg_1HAP	67	115	82	264
3Ni–4Co/Mg_1HAP	67	107	70	244
3Ni–5Co/Mg_1HAP	54	98	58	210

desorption peaks, I, II, and III, in the temperature range of 25–600 °C, corresponding to the weakly basic site (25–150 °C), the moderately basic site (150 °C) and the strongly basic site (300 °C), respectively, of the catalyst. The weak basic site of type I represents the weak adsorption of CO_2 by the catalyst, which is usually physical adsorption and is mainly distributed on the surface of the catalyst or in the pores of the catalyst; additionally, this part of the CO_2 will be desorbed at lower temperatures. Types II and III correspond to moderate and strong basic sites on the surface of the catalyst, respectively. These two basic sites are beneficial for the adsorption and activation of CO_2 during the dry reforming of methane [59,60] and are closely related to the resistance of the catalyst to carbon deposition.

The CO_2 desorption amounts of several catalysts with different Ni–Co ratio are listed in Table 3. As shown in Table 3, the addition of Co increased the total amount of CO_2 desorbed from 3Ni/Mg_1HAP. This is mainly due to the strong oxophilicity of the metal Co and the good activation of CO_2, which can promote the adsorption of CO_2. Type I CO_2 is physically adsorbed on the surface of the catalyst, while type II and type III CO_2 are bound to the surface of the catalyst by chemical bonds. 3Ni–1Co/Mg_1HAP shows the highest desorption amount of type II and type III CO_2, corresponding to the strongest CO_2 adsorption capacity and the largest distribution of medium-strong basicity sites, so its anti-carbon deposition ability may be stronger. Nevertheless, the desorption amount of type II and type III CO_2 decreased gradually with increasing Co content in 3Ni-*x*Co/Mg_1HAP. As shown in Fig. S1 in Supplementary Material, the CO_2 desorption amount of the Mg_1HAP support was calculated to be 131 μmol·g^{-1}, which is much lower than that of 3Ni/Mg_1HAP and 3Ni-*x*Co/Mg_1HAP. The characterization of H_2-TPR and XPS showed that when the Co concentration was excessive, the Co entered the lattice of the Mg_1HAP support, which led to a decrease in its ability to adsorb CO_2. In addition, as shown in Table S1, the surface basicity of 3Ni-*x*Co/Mg_1HAP was improved by the addition of Co. The surface basicity of 3Ni-*x*Co/Mg_1HAP increased gradually with increasing Co amount, confirming the contribution of Co to basic sites. Excess Co enters the lattice of Mg_1HAP and cannot be used as a surface basic site to promote the adsorption and activation of CO_2.

3.2. DRM reaction results

The performances of several catalysts were evaluated by a DRM activity test, and the results are shown in Fig. 6 (GHSV = 45000 ml·g^{-1}·h^{-1}, CH_4:CO_2:N_2 = 1:1:1, and ambient atmosphere and reaction at 750 °C). As shown in the diagram, the initial conversions of CO_2 and CH_4 by the 3Ni/Mg_1HAP catalyst and the selectivity of the product are the highest, at 92.3% and 86.1%, respectively. The yield of H_2 was 82.3%, and the ratio of H_2 to CO was 0.91. When the amount of metal Co is 1% or 2%, the conversion of reactants and the selectivity of products improve to a certain extent. The performance of the catalyst is the best when the amount of metal Co is 1%. The initial conversions of CO_2 and CH_4 by the 3Ni–1Co/Mg_1HAP catalyst were 96.40% and 90.17%, respectively. The yields of H_2 and the H_2/CO ratio are 86.2% and 0.94, respectively. The initial conversions of CO_2 and CH_4 by the 3Ni–2Co/Mg_1HAP catalyst are 94.70% and 87.07%, respectively. The yields of H_2 and the H_2/CO ratio are 84.2% and 0.92, respectively. When the amount of metal Co is more than 3%, the activity and stability of the catalyst do not increase but rather decrease compared with the activity and stability of the 3Ni/Mg_1HAP catalyst, which may be due to the decrease in metal dispersion and the formation of large metal particles due to excessive Co, which is not conducive to the DRM reaction [61]. As the active site, Ni sites promote the cleavage of CH_4 to H_2 and C*, while Co sites facilitate the conversion of CO_2 to CO and O*. A smaller metal particle size provides more active sites and contact interfaces, which is more conducive to promoting the activation and cleavage of CO_2 and CH_4. The agglomeration of metal Co and the increase in Co particle size are not conducive to the formation of oxygen species (O*) on the catalyst surface, so the C* produced by the decomposition of CH_4 cannot be oxidized to CO. The residual C* forms carbon deposits on the catalyst surface, thus reducing the stability of the DRM reaction. In addition, the strong oxophylic nature of the metal Co will also lead to the oxidation of active metals, which will also lead to a decrease in catalyst activity. The three catalysts 3Ni–3Co/Mg_1HAP, 3Ni–4Co/Mg_1HAP, and 3Ni–5Co/Mg_1HAP showed a decreasing trend in the conversion of reactants after the fourth hour of the reaction, with initial conversions of CO_2 and CH_4 of 90.1% and 84.7%, 88.1% and 82.0%, 86.6% and 80.8%, respectively; H_2 selectivity and H_2/CO ratio of 80.7% and 0.90, 78.3% and 0.88, 76.3% and 0.87; and conversions of the reactants and selectivity of the products decreasing by approximately 3% on average after 8 h of reaction. For the 3Ni/Mg_1HAP, 3Ni–1Co/Mg_1HAP and 3Ni–2Co/Mg_1HAP catalysts, the activity did not change. In addition, as shown in Table S2, 3Ni–1Co/Mg_1HAP exhibits greater catalytic performance at higher GHSVs than other reported Ni-based catalysts.

The results of the long-term stability tests performed on the 3Ni/Mg_1HAP and 3Ni–1Co/Mg_1HAP catalysts are shown in Fig. 7. The 3Ni–1Co/Mg_1HAP catalyst has good catalytic activity and stability for both CH_4 and CO_2 (Fig. 7(a) and (b)). The initial conversion rate of CO_2 and CH_4 was 96.3% and 89.8%, respectively. After 100 h, the conversion rate of CO_2 and CH_4 was 92.8% and 86.0%, and the inactivation rate of CO_2 and CH_4 was 3.63% and 4.23%, respectively. In addition, the initial CO_2 and CH_4 conversion rate of the 3Ni/Mg_1HAP catalyst was 92.3% and 84.1%. After 100 h, the CO_2 and CH_4 conversion rate was 84.7% and 74.3%, and the inactivation rate of CO_2 and CH_4 was 8.23% and 11.65%, respectively.

Compared with that of the 3Ni/Mg_1HAP catalyst, the inactivation rate of the 3Ni–1Co/Mg_1HAP catalyst is lower at the same time, indicating that the catalyst is more stable, possibly because the addition of metal Co increases the interaction between the metal and support, so the anti-sintering ability of the catalyst is stronger, which avoids the decrease in catalyst activity caused by additional large metal particles; on the other hand, the strong oxophilic nature of metal Co promotes the elimination of graphitic carbon with a stable structure. As shown in Fig. 7(c), the H_2/CO ratio of the 3Ni–1Co/Mg_1HAP catalyst was approximately 0.93 according to the 100 h stability test. In comparison, the H_2/CO ratio of the 3Ni/Mg_1HAP catalyst decreased from 0.92 to 0.88 during the 100 h stability test. When the H_2/CO ratio of the two catalysts is less than 1, side reactions occur during the reaction process. In contrast, the H_2/CO ratio of the 3Ni–1Co/Mg_1HAP catalyst is greater than that of the 3Ni/Mg_1HAP catalyst, indicating that the degree of side reaction is small. Fig. 7(d) shows the carbon balance data. The carbon balance of the 3Ni–1Co/Mg_1HAP and 3Ni/Mg_1HAP catalysts is always

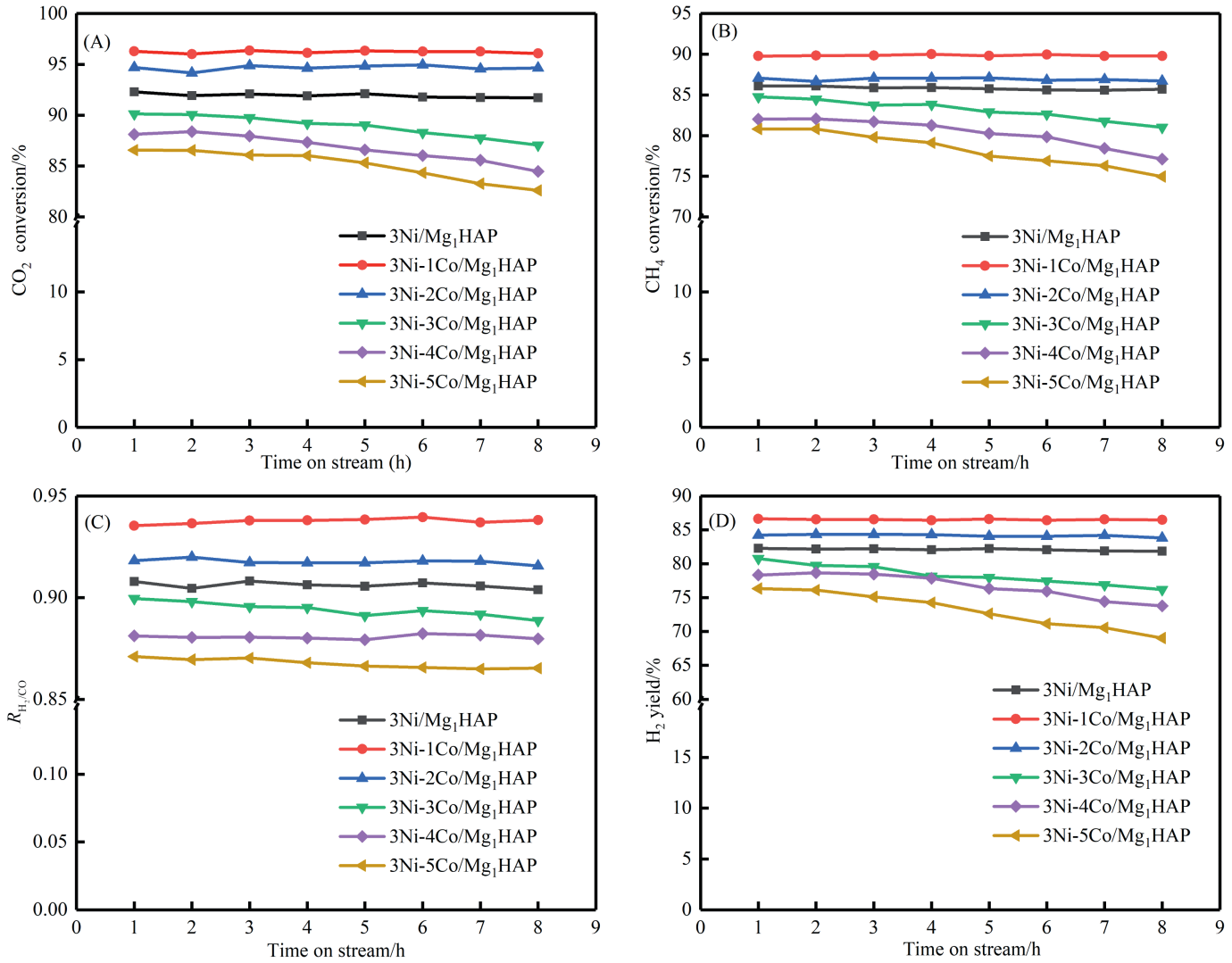

Fig. 6. Catalytic activity of catalysts with different Ni–Co ratio: (a) CO_2 conversion, (b) CH_4 conversion, (c) H_2/CO ratio of the product, and (d) H_2 yield.

between 95% and 98%. However, the carbon balance of the 3Ni–1Co/Mg_1HAP catalyst is greater than that of the 3Ni/Mg_1HAP catalyst, indicating that the less carbon deposited on the 3Ni–1Co/Mg_1HAP catalyst, the greater the stability of the catalyst.

3.3. Carbon deposition analysis

As shown in the XRD patterns (Fig. 1), when the amount of Co is greater than 3%, the amount of Ni^{2+} species at the Ca^{2+} sites on the surface determines the formation of $NiCo_2O_4$, and the amount of Co_3O_4 increases with increasing excess Co. From the XPS spectra (Fig. 4), Ni^{2+} ions enter the lattice of Mg_1HAP to replace the Ca^{2+} [I] and Ca^{2+} [II] sites of Mg_1HAP. Co preferentially interacts with Ni at the Ca^{2+} [II] site and ultimately inhibits the entry and exchange of Ni into the Mg_1HAP lattice. An excess of Co enters the lattice of Mg_1HAP and forms a strong metal-support interaction. Moreover, $NiCo_2O_4$, as a precursor, facilitates the formation of Ni–Co alloys after reduction in H_2/Ar. Ni sites promote the cleavage of CH_4 to H_2 and C*, while Co sites facilitate the conversion of CO_2 to CO and O*. Therefore, the Ni–Co alloy decreases the distance between O* and C* on the surface of 3Ni–1Co/Mg_1HAP, which is conducive to the rapid oxidation of C* by O*, thus inhibiting carbon deposition. However, the excess Co enters the lattice of Mg_1HAP, which decreases the CO_2 adsorption ability and the rate of CO_2 conversion to O*, resulting in the formation of carbon deposits from the accumulated C*.

3.3.1. XRD analysis of the spent catalysts

The fresh 3Ni–1Co/Mg_1HAP was reduced in H_2/Ar before the DRM reaction. To reveal the change of the spent 3Ni–1Co/Mg_1HAP after 100 h of the stability test, the XRD pattern of the reduced 3Ni–1Co/Mg_1HAP was added for comparison, as shown in Fig. 8. Compared with those in the spectrum of fresh 3Ni–1Co/Mg_1HAP, a large number of new peaks were observed in the spectrum of reduced 3Ni–1Co/Mg_1HAP, which were mainly attributed to $Ca_{18}Mg_2H_2(PO_4)_{14}$ (PDF#702064). The formation of $Ca_{18}Mg_2H_2(PO_4)_{14}$ is attributed to the entry of H_2 into the lattice of HAP during the reduction in H_2/Ar. Moreover, the peaks of $Ca_{10}(PO_4)_6(OH)_2$ (PDF#75—05665) could also be found in the XRD pattern of reduced 3Ni–1Co/Mg_1HAP. Notably, the peak at 44.4° corresponds to Ni^0 (PDF#87—0712), indicating the generation of Ni^0 metal after the reduction in H_2/Ar. Furthermore, the diffraction peaks of spent 3Ni–1Co/Mg_1HAP are similar to those of reduced 3Ni–1Co/Mg_1HAP, confirming the excellent stability of

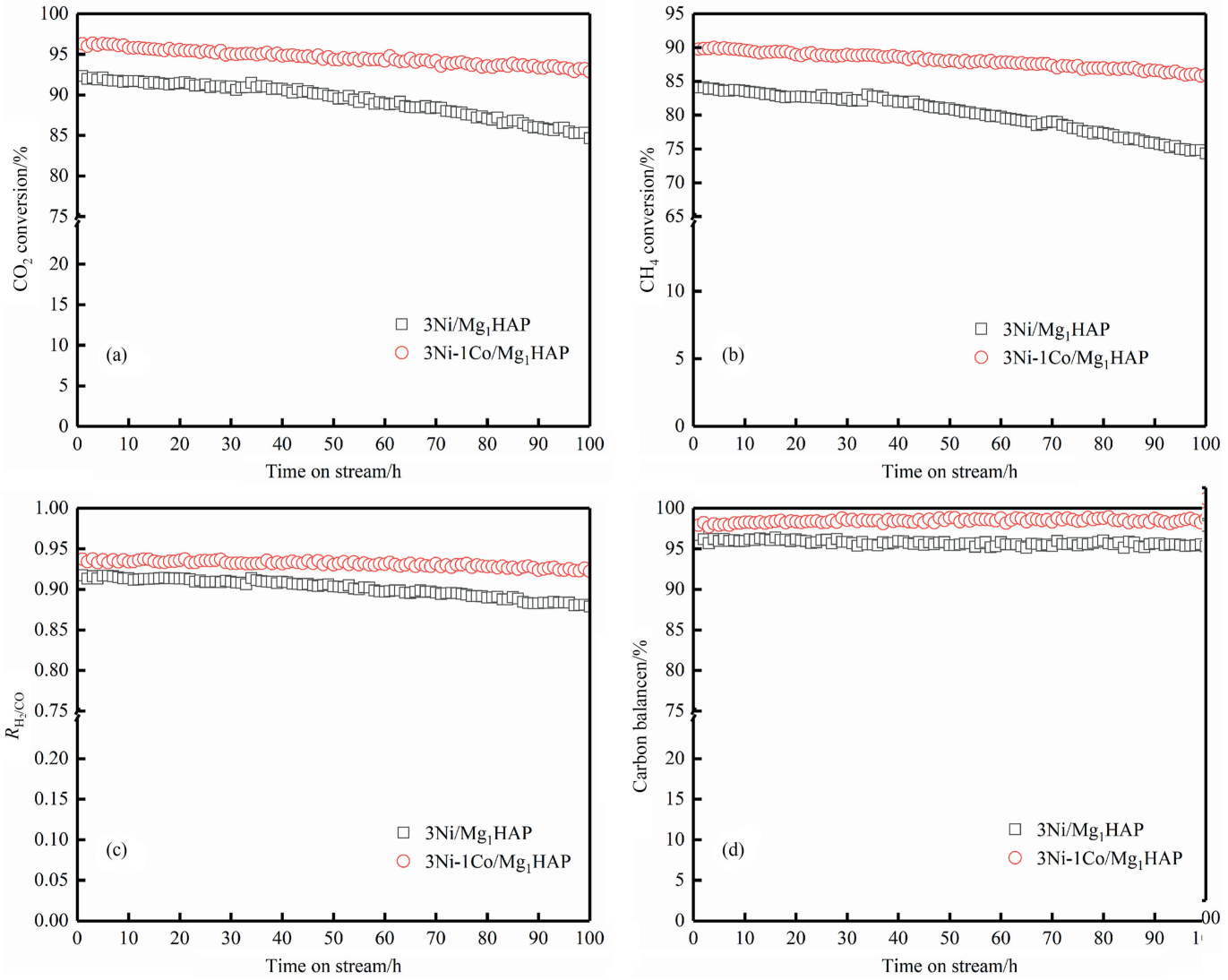

Fig. 7. Stability test of the 3Ni/Mg_1HAP and 3Ni−1Co/Mg_1HAP catalysts. (a) CO_2 conversion, (b) CH_4 conversion, (c) H_2/CO ratio of the product, and (d) carbon balance.

reduced 3Ni−1Co/Mg_1HAP. According to the Scherrer equation, the approximate FWHM indicates that the crystal grain size does not change significantly before and after 100 h of DRM. As shown in Fig. 8 (b), which is the enlarged region from 25° to 27° in Fig. 8 (a), the peak at 26.62° is attributed to graphitic carbon (PDF#75—1621), indicating the production of carbon deposits on the surface of spent 3Ni−1Co/Mg_1HAP after 100 h of DRM reaction [29].

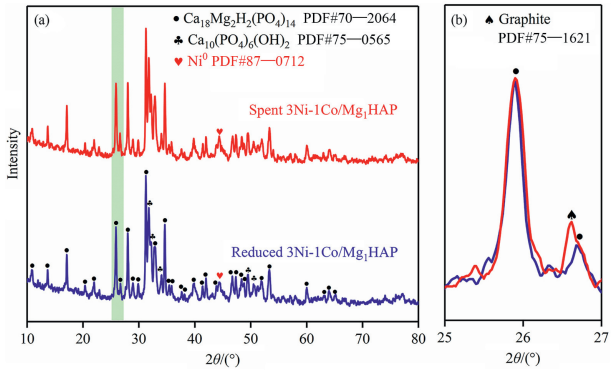

Fig. 8. (a) XRD patterns of reduced 3Ni−1Co/Mg_1HAP and spent 3Ni−1Co/Mg_1HAP after 100 h of stability test. (b) Enlarged region from 25° to 27° in Fig. 8 (a).

3.3.2. *Raman spectral analysis of the catalysts after the stability test*

To understand the type of carbon deposition formed after the stability test of 3Ni/Mg_1HAP and 3Ni−1Co/Mg_1HAP, the Raman spectra of the two catalysts after the stability test were analyzed, as shown in Fig. 9. The Raman spectra shows two main peaks near 1350 and 1580 cm^{-1}, which are the D-band and G-band, respectively. The D band represents the disordered carbon structure of defects, and the G band represents the graphitic carbon structure of sp^2 bonds. The disordered carbon structure is easily oxidized, while the graphitic carbon of the sp^2 bond is not easily oxidized [61,62].

The ratio of the D band to the G band (I_D/I_G) is usually used to measure the graphitization degree of carbon deposition. The higher the I_D/I_G ratio is, the lower the graphitization degree of carbon deposition is [63]. The calculated results show that the I_D/I_G ratio of the 3Ni/Mg_1HAP and 3Ni−1Co/Mg_1HAP catalysts are 0.69 and 0.79, respectively, indicating that the graphitization degree of the 3Ni/Mg_1HAP catalyst is greater, carbon deposition is not easy to oxidize

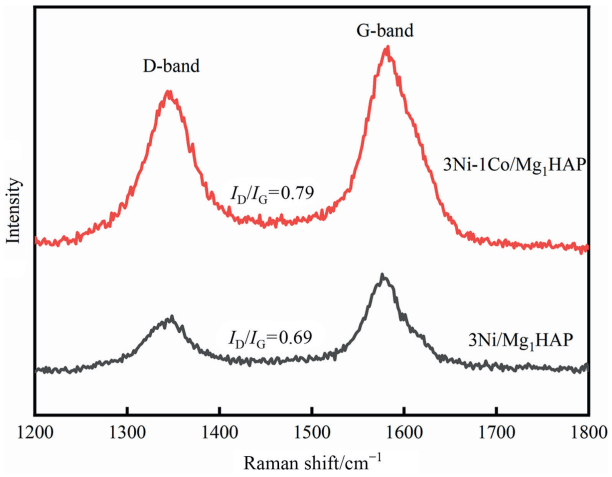

Fig. 9. Raman spectra of the spent 3Ni/Mg_1HAP and 3Ni−1Co/Mg_1HAP catalysts after 100 h of stability test.

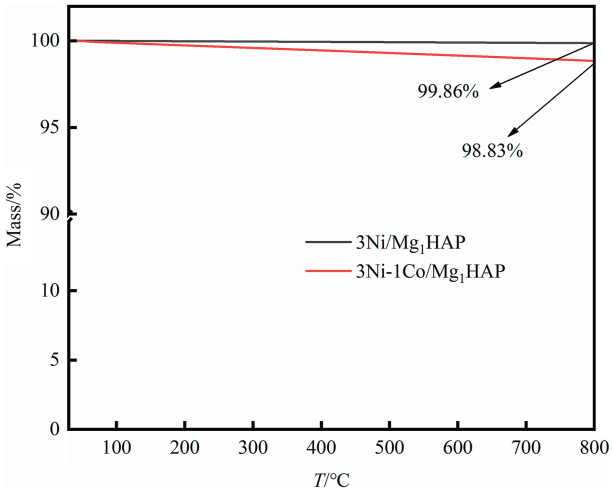

Fig. 10. TG analysis of the 3Ni/Mg_1HAP and 3Ni−1Co/Mg_1HAP catalysts after the stability test.

during the reaction, and the catalyst is more likely to be deactivated, which is the main reason for the decrease in activity.

3.3.3. Thermogravimetric analysis of the catalyst after the stability test

TG tests of the two catalysts after 100 h of reaction were carried out to analyze the amount of carbon deposited after the stability test of the two catalysts. The results are shown in Fig. 10. After 100 h of reaction, the mass loss of the 3Ni/Mg_1HAP and 3Ni−1Co/Mg_1HAP catalysts are 0.14% and 1.17%, respectively. Stability tests revealed that the stability and activity of the 3Ni−1Co/Mg_1HAP catalyst were greater than those of the 3Ni/Mg_1HAP catalyst. Nevertheless, the mass loss of the former is greater than that of the latter, which may be due to the faster dissociation of methane by the former.

The reason why there was no obvious deactivation of the catalyst may be that most of the carbon deposited was amorphous carbon, which does not affect the activity of the catalyst. On the other hand, because 3Ni−1Co/Mg_1HAP consumes lattice oxygen on the surface of the support during the reaction, these lattice oxygens will be supplemented under thermogravimetric conditions [27,64]. For the 3Ni−1Co/Mg_1HAP catalyst, this may be due to the combination of Ni and Co, and Co has a strong oxophilic nature, which leads to the aggregation of oxygen atoms around the Ni−Co alloy; thus, Ni may be oxidized to NiO during the reaction, decreasing the mass gain of the 3Ni−1Co/Mg_1HAP catalyst and increasing mass loss.

4. Conclusions

Ni−Co/Mg_1HAP catalysts with different Ni−Co ratio were synthesized by the coprecipitation method. The formation of the Ni−Co alloy was confirmed by XRD and XPS analysis. H_2-TPR confirmed that the addition of Co improved the interactions between the metal and support and between the metal and dispersion. It is worth noting that the catalyst with a Ni−Co ratio of 3:1 has the best performance and excellent long-term stability. Even if the alloy structure is maintained after 100 h of reaction, the conversions of CO_2 and CH_4 by the 3Ni−1Co/Mg_1HAP catalyst are reduced by 3.5% and 3.8%, respectively; the ratio of H_2 to CO is approximately 0.93; and the inactivation rates of the catalyst for the CO_2 and CH_4 conversion are 3.63% and 4.23%, respectively. The conversions of CO_2 and CH_4 by the 3Ni/Mg_1HAP catalyst decreased by 7.6% and 9.8%, respectively. When the ratio of H_2/CO decreased from 0.92 to 0.88, the inactivation rates of the catalysts for the conversion of CO_2 and CH_4 are 8.23% and 11.65%, respectively. The results of Raman and thermogravimetric characterization showed that the 3Ni−1Co/Mg_1HAP catalyst produced less carbon deposition and a greater proportion of amorphous carbon, which was easily oxidized during the DRM stability test. The introduced Co in turn interacts with the exchanged Ni^{2+} species at the Ca^{2+} site to form a Ni−Co alloy, which effectively promotes the cleavage of C−H and C−O, thereby increasing the conversion of CH_4 and CO_2. Moreover, the Ni−Co alloy shortens the distance between O* and C* on the surface of 3Ni−1Co/Mg_1HAP, which is conducive to the rapid oxidation of C* by O*, thus inhibiting carbon deposition.

CRediT Authorship Contribution Statement

Tongming Su: Writing – review & editing, Writing – original draft, Resources, Formal analysis, Data curation. Bo Gong: Writing – original draft, Investigation, Formal analysis, Data curation, Conceptualization. Xinling Xie: Writing – original draft, Methodology, Investigation. Xuan Luo: Writing – review & editing, Resources, Formal analysis. Zuzeng Qin: Writing – review & editing, Writing – original draft, Supervision, Resources, Funding acquisition, Formal analysis. Hongbing Ji: Writing – review & editing, Supervision, Project administration, Methodology.

Declaration of Competing Interest

The authors declare that they have no known competing financial interests or personal relationships that could have appeared to influence the work reported in this paper.

Acknowledgements

This work was supported by the Guangxi Natural Science Foundation (2020GXNSFDA297007), the National Natural Science Foundation of China (22078074), and the Special Funding for ‘Guangxi Bagui Scholars’.

Supplementary Material

Supplementary data to this article can be found online at https://doi.org/10.1016/j.cjche.2024.07.025.

References

[1] A.G. Olabi, M. Ali Abdelkareem, Renewable energy and climate change, *Renew. Sustain. Energy Rev.* 158 (2022) 112111.

[2] A. Munyentwali, H. Li, Q.H. Yang, Review of advances in bifunctional solid acid/base catalysts for sustainable biodiesel production, *Appl. Catal. Gen.* 633 (2022) 118525.

[3] C.W. Mao, Y.X. Chang, X.T. Zhao, X.Y. Dong, Y.F. Geng, N. Zhang, L. Dai, X.W. Wu, L. Wang, Z.X. He, Functional carbon materials for high-performance Zn metal anodes, *J. Energy Chem.* 75 (2022) 135–153.

[4] E. Chamanehpour, M.H. Sayadi, M. Hajiani, A hierarchical graphitic carbon nitride supported by metal–organic framework and copper nanocomposite as a novel bifunctional catalyst with long-term stability for enhanced carbon dioxide photoreduction under solar light irradiation, *Adv. Compos. Hybrid Mater.* 5 (3) (2022) 2461–2477.

[5] S.L. Hamukwaya, Z.Y. Zhao, H.Y. Hao, H.M. Abo-Dief, K.M. Abualnaja, A.K. Alanazi, M.M. Mashingaidze, S.M. El-Bahy, M.N. Huang, Z.H. Guo, Enhanced photocatalytic performance for hydrogen production and carbon dioxide reduction by a mesoporous single-crystal-like TiO_2 composite catalyst, *Adv. Compos. Hybrid Mater.* 5 (3) (2022) 2620–2630.

[6] J.Y. Wang, R. Fu, S.K. Wen, P. Ning, M.H. Helal, M.A. Salem, B.B. Xu, Z.M. El-Bahy, M.N. Huang, Z.H. Guo, L. Huang, Q. Wang, Progress and current challenges for CO_2 capture materials from ambient air, *Adv. Compos. Hybrid Mater.* 5 (4) (2022) 2721–2759.

[7] J.M. Shi, A.G. Wang, Y.L. An, S. Chen, C.Y. Bi, L.N. Qu, C. Shi, F.Y. Kang, C.F. Sun, Z. H. Huang, H.J. Qi, J.G. Hu, Core@shell-structured catalysts based on Mg-O-Cu bond for highly selective photoreduction of carbon dioxide to methane, *Adv. Compos. Hybrid Mater.* 7 (1) (2023) 2.

[8] Q.L.M. Ha, H. Atia, C. Kreyenschulte, H. Lund, S. Bartling, G. Lisak, S. Wohlrab, U. Armbruster, Effects of modifier (Gd, Sc, La) addition on the stability of low Ni content catalyst for dry reforming of model biogas, *Fuel* 312 (2022) 122823.

[9] Z.P. Zou, T. Zhang, L. Lv, W.X. Tang, G.Q. Zhang, R. Kumar Gupta, Y. Wang, S.W. Tang, Preparation adjacent Ni-Co bimetallic nano catalyst for dry reforming of methane, *Fuel* 343 (2023) 128013.

[10] X.T. Cui, S.K. Kær, A comparative study on three reactor types for methanol synthesis from syngas and CO_2, *Chem. Eng. J.* 393 (2020) 124632.

[11] J. Yang, W.P. Ma, D. Chen, A. Holmen, B.H. Davis, Fischer–Tropsch synthesis: a review of the effect of CO conversion on methane selectivity, *Appl. Catal. Gen.* 470 (2014) 250–260.

[12] Y.L. Huang, X.D. Li, Q. Zhang, V.A. Vinokurov, W. Huang, Enhanced carbon tolerance of hydrotalcite-derived Ni-Ir/Mg(Al)O catalysts in dry reforming of methane under elevated pressures, *Fuel Process. Technol.* 237 (2022) 107446.

[13] T. Kobayashi, T. Furuya, H. Fujitsuka, T. Tago, Synthesis of Birdcage-type zeolite encapsulating ultrafine Pt nanoparticles and its application in dry reforming of methane, *Chem. Eng. J.* 377 (2019) 120203.

[14] Z.Y. Liu, F. Zhang, N. Rui, X. Li, L.L. Lin, L.E. Betancourt, D. Su, W.Q. Xu, J.J. Cen, K. Attenkofer, H. Idriss, J.A. Rodriguez, S.D. Senanayake, Highly active ceria-supported Ru catalyst for the dry reforming of methane: *In situ* identification of $Ru^{\delta+}$–Ce^{3+} interactions for enhanced conversion, *ACS Catal.* 9 (4) (2019) 3349–3359.

[15] R.K. Singha, A. Shukla, A. Sandupatla, G. Deo, R. Bal, Synthesis and catalytic activity of a Pd doped Ni–MgO catalyst for dry reforming of methane, *J. Mater. Chem. A* 5 (30) (2017) 15688–15699.

[16] J. Wu, L.Y. Qiao, Z.F. Zhou, G.J. Cui, S.S. Zong, D.J. Xu, R.P. Ye, R.P. Chen, R. Si, Y. G. Yao, Revealing the synergistic effects of Rh and substituted $La_2B_2O_7$ (B = Zr or Ti) for preserving the reactivity of catalyst in dry reforming of methane, *ACS Catal.* 9 (2) (2019) 932–945.

[17] Y. Fu, W. Kong, B. Pan, C. Yuan, S. Li, H. Zhu, J. Zhang, In situ redispersion of rhodium nanocatalyst for CO_2 reforming of CH_4, *J. Environ. Chem. Eng.* 9 (4) (2021) 105790.

[18] W.J. Jang, J.O. Shim, H.M. Kim, S.Y. Yoo, H.S. Roh, A review on dry reforming of methane in aspect of catalytic properties, *Catal. Today* 324 (2019) 15–26.

[19] Y. Xu, X.H. Du, J. Li, P. Wang, J. Zhu, F.J. Ge, J. Zhou, M. Song, W.Y. Zhu, A comparison of Al_2O_3 and SiO_2 supported Ni-based catalysts in their performance for the dry reforming of methane, *J. Fuel Chem. Technol.* 47 (2) (2019) 199–208.

[20] M.A. Khan, M.S. Challiwala, A.V. Prakash, N.O. Elbashir, Conceptual modeling of a reactor bed of a nickel-copper bi-metallic catalyst for dry reforming of methane, *Chem. Eng. Sci.* 267 (2023) 118315.

[21] P.B. Kurmashov, A.G. Bannov, M.V. Popov, A.E. Brester, A.V. Ukhina, A.V. Ishchenko, E.A. Maksimovskii, L.I. Tolstobrova, A.O. Chulkov, G.G. Kuvshinov, CO_x-free catalytic decomposition of methane over solution combustion synthesis derived catalyst: synthesis of hydrogen and carbon nanofibers, *Int. J. Energy Res.* 46 (9) (2022) 11957–11971.

[22] L. Yao, J. Shi, H.L. Xu, W. Shen, C.W. Hu, Low-temperature CO_2 reforming of methane on Zr-promoted Ni/SiO_2 catalyst, *Fuel Process. Technol.* 144 (2016) 1–7.

[23] Y. Kathiraser, U. Oemar, E.T. Saw, Z.W. Li, S. Kawi, Kinetic and mechanistic aspects for CO_2 reforming of methane over Ni based catalysts, *Chem. Eng. J.* 278 (2015) 62–78.

[24] M. Grabchenko, G. Pantaleo, F. Puleo, T.S. Kharlamova, V.I. Zaikovskii, O. Vodyankina, L.F. Liotta, Design of Ni-based catalysts supported over binary La-Ce oxides: influence of La/Ce ratio on the catalytic performances in DRM, *Catal. Today* 382 (2021) 71–81.

[25] P.K. Chaudhary, G. Deo, Process and catalyst improvements for the dry reforming of methane, *Chem. Eng. Sci.* 276 (2023) 118767.

[26] R.L.B.A. Medeiros, G.P. Figueredo, H.P. Macedo, Â.A.S. Oliveira, R.C. Rabelo-Neto, D.M.A. Melo, R.M. Braga, M.A.F. Melo, One-pot microwave-assisted combustion synthesis of Ni-Al_2O_3 nanocatalysts for hydrogen production *via* dry reforming of methane, *Fuel* 287 (2021) 119511.

[27] J.G. Meng, W. Pan, T.T. Gu, C.S. Bu, J.B. Zhang, X.Y. Wang, C.Q. Liu, H. Xie, G.L. Piao, One-pot synthesis of a highly active and stable Ni-embedded hydroxyapatite catalyst for syngas production *via* dry reforming of methane, *Energy Fuels* 35 (23) (2021) 19568–19580.

[28] L. Baharudin, A.C.K. Yip, V. Golovko, M.J. Watson, Potential of metal monoliths with grown carbon nanomaterials as catalyst support in intensified steam reformer: a perspective, *Rev. Chem. Eng.* 36 (4) (2020) 459–491.

[29] C.Y. Jiang, M.R. Akkullu, B. Li, J.C. Davila, M.J. Janik, K.M. Dooley, Rapid screening of ternary rare-earth–Transition metal catalysts for dry reforming of methane and characterization of final structures, *J. Catal.* 377 (2019) 332–342.

[30] J. Wang, Y.R. Mao, L.Z. Zhang, Y.L. Li, W.M. Liu, Q.X. Ma, D.S. Wu, H.G. Peng, Remarkable basic-metal oxides promoted confinement catalysts for CO_2 reforming, *Fuel* 315 (2022) 123167.

[31] X.L. He, D.Q. Zeng, Y.M. Liu, Q. Chen, J.R. Yang, R.C. Gao, T. Fujita, Y.Z. Wei, Porous Co_xP nanosheets decorated $Mn_{0.35}Cd_{0.65}S$ nanoparticles for highly enhanced noble-metal-free photocatalytic H_2 generation, *J. Colloid Interface Sci.* 625 (2022) 859–870.

[32] F.G. Wang, K.H. Han, L.L. Xu, H. Yu, W.D. Shi, Ni/SiO_2 catalyst prepared by strong electrostatic adsorption for a low-temperature methane dry reforming reaction, *Ind. Eng. Chem. Res.* 60 (8) (2021) 3324–3333.

[33] S. De, J.G. Zhang, R. Luque, N. Yan, Ni-based bimetallic heterogeneous catalysts for energy and environmental applications, *Energy Environ. Sci.* 9 (11) (2016) 3314–3347.

[34] Z. Bian, S. Das, M.H. Wai, P. Hongmanorom, S. Kawi, A review on bimetallic nickel-based catalysts for CO_2 reforming of methane, *ChemPhysChem* 18 (22) (2017) 3117–3134.

[35] S.N.A. Rosli, S.Z. Abidin, O.U. Osazuwa, X.L. Fan, Y.L. Jiao, The effect of oxygen mobility/vacancy on carbon gasification in nano catalytic dry reforming of methane: a review, *J. CO_2 Util.* 63 (2022) 102109.

[36] D.L. Li, S.P. Xu, K. Song, C.Q. Chen, Y.Y. Zhan, L.L. Jiang, Hydrotalcite-derived Co/Mg(Al)O as a stable and coke-resistant catalyst for low-temperature carbon dioxide reforming of methane, *Appl. Catal. Gen.* 552 (2018) 21–29.

[37] X.L. Fan, Z.T. Liu, Y.A. Zhu, G.S. Tong, J.D. Zhang, C. Engelbrekt, J. Ulstrup, K.K. Zhu, X.G. Zhou, Tuning the composition of metastable $Co_xNi_yMg_{100-x-y}(OH)(OCH_3)$ nanoplates for optimizing robust methane dry reforming catalyst, *J. Catal.* 330 (2015) 106–119.

[38] B. Erdogan, H. Arbag, N. Yasyerli, SBA-15 supported mesoporous Ni and Co catalysts with high coke resistance for dry reforming of methane, *Int. J. Hydrog. Energy* 43 (3) (2018) 1396–1405.

[39] B. AlSabban, L. Falivene, S.M. Kozlov, A. Aguilar-Tapia, S. Ould-Chikh, J.L. Hazemann, L. Cavallo, J.M. Basset, K. Takanabe, In-operando elucidation of bimetallic CoNi nanoparticles during high-temperature CH_4/CO_2 reaction, *Appl. Catal. B Environ.* 213 (2017) 177–189.

[40] K.F. Sheng, D. Luan, H. Jiang, F. Zeng, B. Wei, F. Pang, J.P. Ge, Ni_xCo_y nanocatalyst supported by ZrO_2 hollow sphere for dry reforming of methane: synergetic catalysis by Ni and co in alloy, *ACS Appl. Mater. Interfaces* 11 (27) (2019) 24078–24087.

[41] M.A. Vasiliades, P. Djinović, A. Pintar, J. Kovač, A.M. Efstathiou, The effect of CeO_2–ZrO_2 structural differences on the origin and reactivity of carbon formed during methane dry reforming over NiCo/CeO_2–ZrO_2 catalysts studied by transient techniques, *Catal. Sci. Technol.* 7 (22) (2017) 5422–5434.

[42] M.A. Vasiliades, C.M. Damaskinos, P. Djinović, A. Pintar, A.M. Efstathiou, Dry reforming of CH_4 over NiCo/$Ce_{0.75}Zr_{0.25}O_{2-\delta}$: the effect of CO on the site activity and carbon pathways studied by transient techniques, *Catal. Commun.* 149 (2021) 106237.

[43] M.A. Vasiliades, C.M. Damaskinos, P. Djinović, A. Pintar, A.M. Efstathiou, A transient isotopic study for investigating important design parameters of NiCo/$Ce_{0.75}Zr_{0.25}O_{2-\delta}$ catalyst for the dry reforming of methane, *Catal. Commun.* 178 (2023) 106674.

[44] B. Gong, T.M. Su, X.L. Xie, H.B. Ji, Z.Z. Qin, Promotional effects of Mg-substituted Ni/Mg_xHAP catalysts on carbon resistance during dry reforming of methane, *Ind. Eng. Chem. Res.* 62 (33) (2023) 12935–12948.

[45] C.S. Wang, T.M. Su, Z.Z. Qin, H.B. Ji, Coke-resistant Ni-based bimetallic catalysts for the dry reforming of methane: effects of indium on the Ni/Al_2O_3 catalyst, *Catal. Sci. Technol.* 12 (15) (2022) 4826–4836.

[46] J. Horlyck, C. Lawrey, E.C. Lovell, R. Amal, J. Scott, Elucidating the impact of Ni and Co loading on the selectivity of bimetallic NiCo catalysts for dry reforming of methane, *Chem. Eng. J.* 352 (2018) 572–580.

[47] J. Horlyck, M. Sara, E.C. Lovell, R. Amal, J. Scott, Effect of metal-support interactions in mixed Co/Al catalysts for dry reforming of methane, *ChemCatChem* 11 (15) (2019) 3432–3440.

[48] I.V. Zagaynov, A.S. Loktev, A.L. Arashanova, V.K. Ivanov, A.G. Dedov, I.I. Moiseev, Ni(Co)–$Gd_{0.1}Ti_{0.1}Zr_{0.1}Ce_{0.7}O_2$ mesoporous materials in partial oxidation and dry reforming of methane into synthesis gas, *Chem. Eng. J.* 290 (2016) 193–200.

[49] Q. Song, R. Ran, X.D. Wu, Z.C. Si, D. Weng, Dry reforming of methane over Ni catalysts supported on micro- and mesoporous silica, *J. CO_2 Util.* 68 (2023) 102387.
[50] Y.X. Lin, C. Yang, W. Zhang, H. Machida, K. Norinaga, Lattice Boltzmann study on the effect of hierarchical pore structure on fluid flow and coke formation characteristics in open-cell foam for dry reforming of methane, *Chem. Eng. Sci.* 268 (2023) 118380.
[51] Z. Boukha, M. Kacimi, M.F.R. Pereira, J.L. Faria, J.L. Figueiredo, M. Ziyad, Methane dry reforming on Ni loaded hydroxyapatite and fluoroapatite, *Appl. Catal. Gen.* 317 (2) (2007) 299–309.
[52] J.H. Park, S. Yeo, T.J. Kang, I. Heo, K.Y. Lee, T.S. Chang, Enhanced stability of Co catalysts supported on phosphorus-modified Al_2O_3 for dry reforming of CH_4, *Fuel* 212 (2018) 77–87.
[53] X.M. Lei, X.Z. Du, H. Xin, X.Q. Chen, H.R. Yang, L.Y. Zhou, Y. Zeng, H.L. Zhang, Y. F. Tian, D. Li, C.W. Hu, Chemical-switching strategy for the production of green biofuel on NiCo/MCM-41 catalysts by tuning atmosphere, *Fuel* 315 (2022) 123118.
[54] K. Liu, F.L. Xing, Y.Y. Xiao, N. Yan, K.I. Shimizu, S. Furukawa, Development of a highly stable ternary alloy catalyst for dry reforming of methane, *ACS Catal.* 13 (6) (2023) 3541–3548.
[55] L.L. Wang, G.G. Tang, S. Liu, H.L. Dong, Q.Q. Liu, J.F. Sun, H. Tang, Interfacial active-site-rich 0D Co_3O_4/1D TiO_2 *p-n* heterojunction for enhanced photocatalytic hydrogen evolution, *Chem. Eng. J.* 428 (2022) 131338.
[56] Y.X. Shi, L.L. Li, Z. Xu, F. Guo, W.L. Shi, Construction of full solar-spectrum available S-scheme heterojunction for boosted photothermal-assisted photocatalytic H_2 production, *Chem. Eng. J.* 459 (2023) 141549.
[57] C. Han, X.D. Zhang, S.S. Huang, Y. Hu, Z. Yang, T.T. Li, Q.P. Li, J.J. Qian, MOF-on-MOF-derived hollow Co_3O_4/In_2O_3 nanostructure for efficient photocatalytic CO_2 reduction, *Adv. Sci.* 10 (19) (2023) e2300797.
[58] J.N. Xin, H.J. Cui, Z.M. Cheng, Z.M. Zhou, Bimetallic Ni-Co/SBA-15 catalysts prepared by urea co-precipitation for dry reforming of methane, *Appl. Catal. Gen.* 554 (2018) 95–104.
[59] M. Abbas, U. Sikander, M.T. Mehran, S.H. Kim, Exceptional stability of hydrotalcite derived spinel $Mg(Ni)Al_2O_4$ catalyst for dry reforming of methane, *Catal. Today* 403 (2022) 74–85.
[60] A.N.T. Cao, C.Q. Pham, T.M. Nguyen, T. Van Tran, P.T.T. Phuong, D.V.N. Vo, Dysprosium promotion on Co/Al_2O_3 catalysts towards enhanced hydrogen generation from methane dry reforming, *Fuel* 324 (2022) 124818.
[61] Y. Kwon, J.E. Eichler, C.B. Mullins, $NiAl_2O_4$ as a beneficial precursor for Ni/Al_2O_3 catalysts for the dry reforming of methane, *J. CO_2 Util.* 63 (2022) 102112.
[62] J.C.S. Araújo, A.L.G. Pinheiro, A.C. Oliveira, M.G.A. Cruz, J.M.C. Bueno, R.S. Araujo, R. Lang, Catalytic assessment of nanostructured Pt/*x*La_2O_3-Al_2O_3 oxides for hydrogen production by dry reforming of methane: effects of the lanthana content on the catalytic activity, *Catal. Today* 349 (2020) 141–149.
[63] J. Sun, D. Yamaguchi, L.G. Tang, S. Periasamy, H.Y. Ma, J.N. Hart, C.A. Ken, Enhancement of oxygen exchanging capability by loading a small amount of ruthenium over ceria-zirconia on dry reforming of methane, *Adv. Powder Technol.* 33 (2) (2022) 103407.
[64] J.G. Meng, T.T. Gu, W. Pan, C.S. Bu, J.B. Zhang, X.Y. Wang, C.Q. Liu, H. Xie, G.L. Piao, Promotional effects of defects on Ni/HAP catalyst for carbon resistance and durability during dry reforming of methane, *Fuel* 310 (2022) 122363.